# Microstructural Control of Physical Properties During Deformation of Porous Limestone

Nicolas Brantut, Madeline Baker, Lars Hansen, Patrick Baud

Journal of Geophysical Research: Solid Earth

RESEARCH ARTICLE
10.1029/2018JB015636

# Microstructural Control of Physical Properties During Deformation of Porous Limestone

**Nicolas Brantut**[1], **Madeline Baker**[1], **Lars N. Hansen**[2], **and Patrick Baud**[3]

[1]Rock and Ice Physics and Seismological Laboratory, Department of Earth Sciences, University College London, London, UK, [2]Rock Rheology Laboratory, Department of Earth Sciences, University of Oxford, Oxford, UK, [3]Laboratoire de Géophysique Expérimentale, École et Observatoire des Sciences de la Terre, CNRS UMR 7516, Université de Strasbourg, Strasbourg, France

**Key Points:**
- Compaction deformation produces a moderate permeability reduction in Purbeck limestone (13% porosity)
- Deformation induces strong decreases in *P* and *S* wave speeds, as well as a strong anelliptic anisotropy
- In porous limestones, porosity, permeability, and wave velocities evolve during deformation but in response to distinct microscale processes

**Correspondence to:**
N. Brantut,
n.brantut@ucl.ac.uk

**Citation:**
Brantut, N., Baker, M., Hansen, L. N., & Baud, P. (2018). Microstructural control of physical properties during deformation of porous limestone. *Journal of Geophysical Research: Solid Earth*, *123*. https://doi.org/10.1029/2018JB015636

Received 8 FEB 2018
Accepted 28 MAY 2018
Accepted article online 5 JUN 2018

**Abstract** We performed triaxial deformation experiments in Purbeck limestone (13.8% average porosity) across the brittle-ductile transition and monitored the evolution of permeability and wave velocities as a function of strain. In the brittle regime, the rock yields in dilation. In the ductile regime, the rock first yields in compaction and then undergoes net dilation at some critical level of strain. The permeability increases after failure in the brittle regime and decreases with increasing compaction in the ductile regime. The wave velocities decrease with increasing strain, and the material becomes transversely isotropic. At axial strains of the order of 5%, the anisotropy parameters (from Thomsen, 1986) are around $\epsilon \approx -0.2$ and $\delta \approx -0.3$. Under hydrostatic conditions, the rock also yields in compaction. The hydrostatic yield point is not marked by any significant drop or increase in wave velocity during loading, but wave velocities decrease (and therefore crack density increases) significantly upon unloading. In all our tests, the permeability change is proportional to the initial porosity change until the point of net dilation is reached. The strain at that point also acts as a scaling factor for the relative drop in *P* and *S* wave velocities during deformation. All our experimental data point to a disconnection between the evolution of permeability, porosity, and wave velocities during deformation in the ductile regime: permeability is controlled by a fraction of the micropore network, while wave velocities are mostly influenced by microcracks that do not contribute significantly to either the total rock porosity or fluid flow properties.

## 1. Introduction

With the development of 4-D seismic monitoring of reservoirs and $CO_2$ injection in carbonate formations (Angerer et al., 2002; Grochau et al., 2014), a fundamental understanding of the concomitant evolution of elastic wave velocity and petrophysical attributes of carbonate rocks at in situ conditions is necessary. Such knowledge hinges on rock mechanics experiments to describe how inelastic deformation could impact rock properties in various field situations. The coupling between deformation and physical properties in porous sandstones is now well understood following a series of studies in the last decades (e.g., Baud et al., 2012; Fortin et al., 2007; Zhu & Wong, 1997). There is, however, a paucity of data investigating similar coupling in limestone.

The diagenetic processes leading to the formation of carbonate rocks often result in complex microstructures. One notable feature of porous carbonates is that their porosity often shows a bimodal distribution in terms of pore size, with a network of macropores (typically >10 μm in diameter) occurring within a microporous matrix or in between microporous allochems (ooliths or peloids), with submicron pore sizes (e.g., Anselmetti et al., 1998; Choquette & Pray, 1970; Pittman, 1971). This dual porosity has strong implications for the physical properties and mechanical behavior of porous carbonates. For instance, Baechle et al. (2008) showed that the microporosity exerts a strong control on the elastic wave velocities and on the fluid flow properties of carbonates. Regarding mechanical properties, Zhu et al. (2010) showed that the microporosity within the allochems and cement is where microcrack damage initiates, leading to the collapse of macropores during deformation in the cataclastic flow regime. The mechanical behavior of porous carbonates is further complicated by their microscale heterogeneity: Dautriat et al. (2011) and Vajdova et al. (2012) showed that deformation is strongly heterogeneous and partitioned between the constitutive elements of the rock (cement, micrite, and allochems). In oolithic limestones, Regnet et al. (2015) demonstrated that the distribution of microporosity

exerts a strong influence on the macroscale mechanical behavior. Recently, Baud, Exner, et al. (2017) showed the degree of cementation could also be at the origin of large variability in mechanical strength and could promote or inhibit different localized failure modes during compaction of carbonates.

Despite their microstructural complexity, from a phenomenological point of view the macroscopic mechanical behavior of carbonate rocks is relatively well understood. In both micritic and allochemical limestones, Baud et al. (2000) and Vajdova et al. (2004) showed that yielding at elevated confining pressure occurs by shear enhanced compaction, followed at larger strains by net dilation. Environmental conditions have a significant effect on the strength of carbonates. The presence of water (as opposed to dry conditions) tends to promote an earlier onset of inelastic deformation in both the brittle (Nicolas et al., 2016) and ductile regime (Lisabeth & Zhu, 2015). Furthermore, elevated temperatures tend to shift the brittle-ductile transition toward lower confining pressure (Lisabeth & Zhu, 2015; Nicolas et al., 2016). The deformation of limestone is also strongly time dependent: brittle creep and time-dependent failure was evidenced in both water-saturated and dry carbonates (Brantut et al., 2014b; Nicolas et al., 2017).

Regarding physical properties and their evolution during deformation, the available data are more scarce. Lisabeth and Zhu (2015) measured permeability during deformation of Indiana Limestone and found a significant decrease by typically a factor of 5 after the first few percent strain in the cataclastic flow regime, irrespective of the fluid composition and overall sample strength. Brantut et al. (2014b) and Nicolas et al. (2016) measured changes in elastic wave velocities during brittle and semibrittle deformation of Purbeck Limestone (a grainstone with sparry calcite cement) and Tavel Limestone (a porous micrite), respectively, and determined that deformation is associated with strong decreases in *P* and *S* wave velocities. Such changes can be attributed to the growth of microcracks, which eventually leads to failure in the brittle regime. More recently, Baud, Schubnel et al. (2017) showed that inelastic compaction in a high-porosity limestone resulted first in a decrease of *P* wave velocity due to microcacking (grain crushing), followed after a few percent of inelastic strain by an increase of Vpdue to porosity reduction.

Despite the few recent studies mentioned above, the evolution of permeability and elastic wave velocities during deformation remains unknown in porous carbonates, especially in the ductile regime. In addition to providing essential rock properties during deformation, the combined measurement of transport and elastic properties also has the potential to lead to invaluable understanding of the microphysical processes operating during cataclastic deformation. Of particular interest is the influence of the pore size distribution of the evolution of the rock physical properties as deformation proceeds.

In this paper, we present the results from a series of triaxial deformation experiments conducted on Purbeck Limestone at effective confining pressures ranging from 10 to 80 MPa, spanning the brittle to ductile transition. An additional experiment was performed in purely hydrostatic conditions up to 160 MPa effective confining pressure. We used decane as a pore fluid to minimize complications arising from fluid-rock interactions. Permeability and elastic wave speeds were measured repeatedly throughout the experiments, and we conducted detailed microstructural analysis of the deformed samples. The combination of all our data allows us to develop a complete micromechanical understanding of the deformation processes, highlighting the crucial role of microcracks and micropores in the mechanical behavior and in the transport properties of the rock.

## 2. Starting Material and Methods

The material used in this study was Pond freestone Purbeck limestone (Dorset, UK). This rock is a grainstone composed of 80% calcite and 20% quartz. The allochems are mostly peloids made of microcrystalline calcite, and the cement is made of sparry calcite. Quartz appears as chert nodules. The initial porosity of Purbeck limestone is on average 13.8%, and the permeability is around $2 \times 10^{-16}$ m$^2$ (Brantut et al., 2014b).

Cylindrical samples 40 mm in diameter and 100 mm in length were cored from one block in a direction perpendicular to the apparent bedding plane. The samples' ends were ground flat to ensure parallelism of the loading surfaces. The samples were then ovendried for at least 48 hr at 60°C. Prior to each experiment, the samples were held under vacuum for several hours and subsequently saturated with decane.

The decane-saturated samples were inserted into a viton jacket and placed in a triaxial deformation apparatus installed in the Rock and Ice Physics Laboratory at University College London (see full description in Eccles et al., 2005). In this machine, the confining pressure is applied with silicon oil and controlled within

a 0.4 MPa accuracy by an electric pump. Inside the pressure vessel, the sample is positioned between two steel end caps that accommodate pore fluid ports, connected at one end to a servocontrolled intensifier and at the other end to a blank. The fluid pressure is monitored on each side by a pressure transducer (with a precision of the order of $10^{-3}$ MPa). The fluid volume change inside the intensifier is monitored with a linear variable differential transducer, with a precision of the order of 50 nl. At constant pressure, the fluid volume change in the intensifier corresponds to a pore volume change in the sample (assuming perfect connectivity of all the pore space), which allows us to compute the porosity change of the sample. Assuming that the rock matrix is incompressible, the porosity change also corresponds to the bulk volumetric strain of the sample. The axial deformation is imposed through a piston loaded by a servohydraulic actuator. The applied load is measured with an external load cell and corrected for seal friction during postprocessing. The axial shortening is measured with two external LVDTs and corrected for the elastic deformation of the piston and sample assembly.

For all triaxial deformation experiments, the confining pressure was first raised to 20 MPa, and the pore pressure was then set to 10 MPa at the top end of the sample, while the bottom end was initially kept vented. When a steady flow through the sample was achieved, the bottom end pore fluid circuit was closed and we waited for complete equilibration of both confining and pore pressure. Then, the confining pressure was ramped up to the target pressure of the experiment, which was followed by another equilibration stage. All the deformation experiments were performed under drained conditions, and at a constant axial strain rate of $10^{-5}$ $s^{-1}$. The hydrostatic compaction experiment was conducted at 5 MPa pore pressure, and the confining pressure was increased in steps of 5 to 10 MPa. We systematically waited for the pore volume change to stabilize between each confining pressure step.

In addition to stress, strain and porosity variations, we also measured permeability changes across the sample with the pore pressure oscillation method described by Fischer and Paterson (1992) and Bernabé et al. (2006). A sinusoidal oscillation of the upstream pore pressure of 0.4 MPa in amplitude and 15 s period was superimposed to the constant value (10 MPa for the triaxial experiments and 5 MPa for the hydrostatic compaction experiment), and both the upstream and downstream pore pressures were recorded at a 1 Hz sampling rate. The amplitude ratio and phase lag of the downstream pore pressure was determined by computing spectral ratios of the pore pressure records over moving time windows of 4 min (16 periods) in duration and then inverted for the permeability of the sample. In the inversion procedure, the amplitude ratio and phase lag data are weighted with coefficients of 0.8 and 0.2, respectively, which ensured a stable inversion of all the permeability data. Unfortunately, the storage capacity of the sample could not be retrieved consistently due to the large uncertainty of the method for the parameter range used here.

During the experiments, elastic wave velocity measurements were performed repeatedly with an array of 16 ultrasonic transducers positioned around the samples. Every 2 min, a 250 V high-frequency pulse was sent to each transducer and transmitted signals on the remaining sensors were amplified to 40 dB and recorded at 50 MHz with digital oscilloscopes. For each experiment, arrival times were picked manually on one complete "master" survey, and relative changes in arrival time were obtained automatically for all remaining measurements by using the cross-correlation method described in Brantut et al. (2014a). The absolute error on the wave velocities is of the order of 0.1 km/s, and the relative errors for successive measurements between the same pair of transducers are of the order of 0.1%. The sensor array geometry allowed us to measure *P* wave velocities along ray paths at angles of 90°, 58°, 39°, and 28° from the vertical compression axis, and horizontally polarized *S* wave velocity (*Sh* wave) along the horizontal direction (90° from the compression axis).

## 3. Evolution of Physical Properties During Deformation

The mechanical behavior of Purbeck limestone deformed at effective confining pressures $P_{eff}$ of 10, 30, 40, 50 and 80 MPa is shown in Figure 1. At low effective pressure ($P_{eff} = 10$ MPa), the rock exhibits a typical brittle behavior: the differential stress initially increases, reaches a peak, and drops down to a stable frictional level. The volumetric strain shows linear elastic compaction, followed by dilatancy. The recovered sample was macroscopically fractured. At $P_{eff} = 30$ MPa, the differential stress also exhibits a peak followed by a constant residual stress. The volumetric strain indicates yielding in compaction (marked as C* in Figure 1b) and a subsequent switch to net dilation. At $P_{eff} \geq 40$ MPa, the yield point is always reached in compaction, and strain hardening is systematically observed. With increasing effective pressure, the transition from inelastic

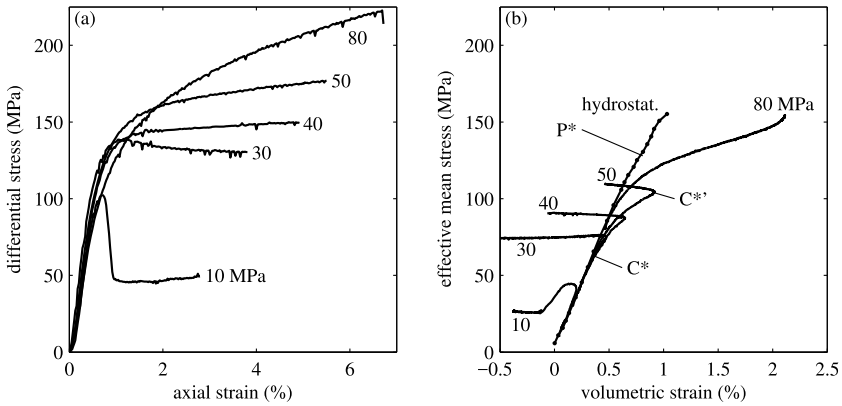


**Figure 1.** Mechanical data from triaxial deformation and hydrostatic compaction experiments in decane-saturated Purbeck limestone. Panel (a) shows the differential stress as a function of axial strain, and panel (b) shows the effective mean stress as a function of volumetric strain. Numbers indicate the effective confining pressure at which experiments were run.

compaction to net dilation (denoted C*′ in Figure 1b) is observed at increasingly larger stress and strain, and more strain hardening is observed. Under hydrostatic loading conditions, the rock yields in compaction (point denoted P*). The yield envelope is shown in Figure 2 and is qualitatively similar to that of all previously tested porous limestones (Wong & Baud, 2012).

The volumetric strain, elastic wave velocities (computed as averages along all the available angles), and permeability measured during hydrostatic compaction are plotted as a function of the effective mean stress in Figure 3. Along the loading branch, both $V_P$ and $V_S$ increase with increasing pressure, from $V_P = 4.42$ km/s and $V_S = 2.44$ km/s at $P_{eff} = 5$ MPa to $V_P = 4.73$ km/s, and $V_S = 2.58$ km/s at $P_{eff} = 155$ MPa. The increase is nonlinear with decreasing rate up to around $P_{eff} = 25$ MPa and becomes almost linear beyond that pressure. At the highest pressure (last data point at $P_{eff} = 155$ MPa), the increase in wave velocity seems to accelerate slightly above the linear trend. During loading, the permeability decreases almost linearly from around $k = 1.1 \times 10^{-16}$ m$^2$ down to $5 \times 10^{-17}$ m$^2$. Along the unloading branch, we observe a strong hysteresis of the volumetric strain, which decreases linearly from 1% at $P_{eff} = 155$ MPa to 0.8% at $P_{eff} = 90$ MPa, well above the volumetric strain of 0.5% observed at the same pressure along the loading branch. The subsequent decrease in volumetric strain is nonlinear, and the final irrecoverable strain (measured at $P_{eff} = 5$ MPa) is 0.2%. The wave velocities also decrease during unloading, initially following the same linear trend as along the loading branch. For $P_{eff} \leq 90$ MPa, the wave velocities decrease nonlinearly below the loading branch and reach $V_P = 4.03$ km/s and $V_S = 2.09$ km/s at $P_{eff} = 5$ MPa, which is markedly below the initial values prior to compaction. The permeability remains almost constant throughout the unloading branch, and its final value is $k = 6 \times 10^{-16}$ m$^2$.

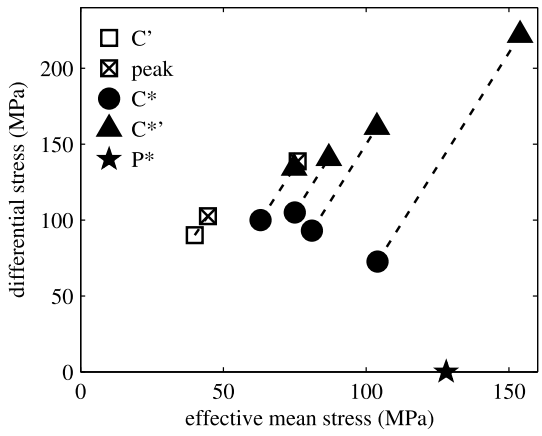


**Figure 2.** Yield envelope for decane-saturated Purbeck limestone. C′ denotes the onset of dilatancy, C* denotes the onset of inelastic compaction, C*′ is the point where net dilation is observed, and P* is the yield point under hydrostatic conditions.

The evolution in *P* and *S* wave velocity during triaxial deformation experiments is plotted as a function of axial strain in Figure 4. In all experiments, $V_P$ and $V_S$ decrease with increasing axial strain beyond the yield point (either C′ in the brittle regime or C* in the ductile regime). The decrease in *P* wave velocity is stronger along the horizontal direction (perpendicular to the compression axis) than along subvertical directions, which indicates the development of elastic anisotropy. The rate and the amplitude of the decrease in wave velocities vary depending on strain and confining pressure. In the brittle regime ($P_{eff} = 10$ MPa, Figure 4a), the wave velocities become constant after the peak stress is achieved and during fault slip. The largest drop in velocity is observed along the horizontal direction, where the postpeak $V_P$ is 3.57 km/s, that is, a 19% decrease compared to the initial value. In the ductile regime ($P_{eff} \geq 30$ MPa), the velocities continuously decrease with increasing strain beyond C*. The rate of decrease is maximum in the first 1% to 2% strain and subsequently decelerates. The rate

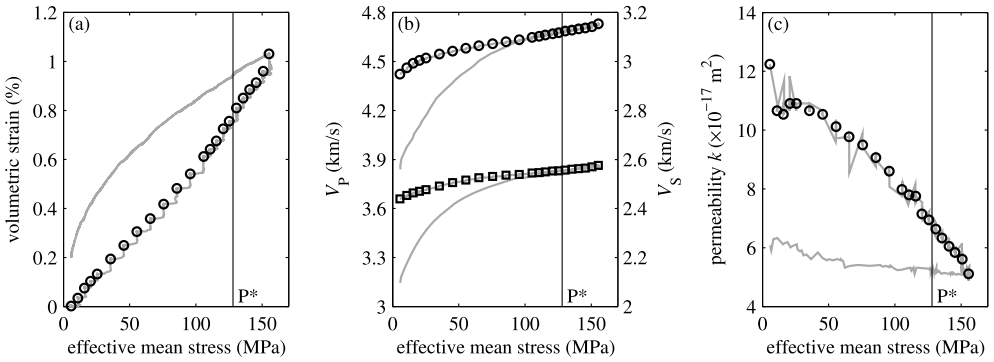


**Figure 3.** Volumetric strain (a), *P* and *S* wave velocity (b), and permeability (c) as a function of effective mean stress during hydrostatic compaction of decane-saturated Purbeck limestone. The continuous grey curve corresponds to the full data record, and the discrete symbols correspond to the data points extracted at the end of each confining pressure step, after equilibration of pressure and strain. The vertical black line marks P*.

of decrease at any given strain also reduces with increasing effective pressure. For instance, at 2% axial strain, the horizontal $V_P$ has dropped by 27% at $P_{eff}$ = 30 MPa, 22% at $P_{eff}$ = 40 MPa, 16% at $P_{eff}$ = 50 MPa, and only 8% at $P_{eff}$ = 80 MPa.

The wave velocity data can be used to extract five independent elastic moduli, assuming a transversely isotropic symmetry. The relationship between wave velocities and elastic moduli $C_{ij}$ (in Voigt's notation) in a transversely isotropic medium is given by (e.g., Thomsen, 1986)

$$\rho V_P^2(\theta) = \frac{1}{2}\left(C_{33} + C_{44} + (C_{11} - C_{33})\sin^2(\theta) + D(\theta)\right), \quad (1)$$

$$\rho V_S^2(\theta) = C_{66}\sin^2(\theta) + C_{44}\cos^2(\theta), \quad (2)$$

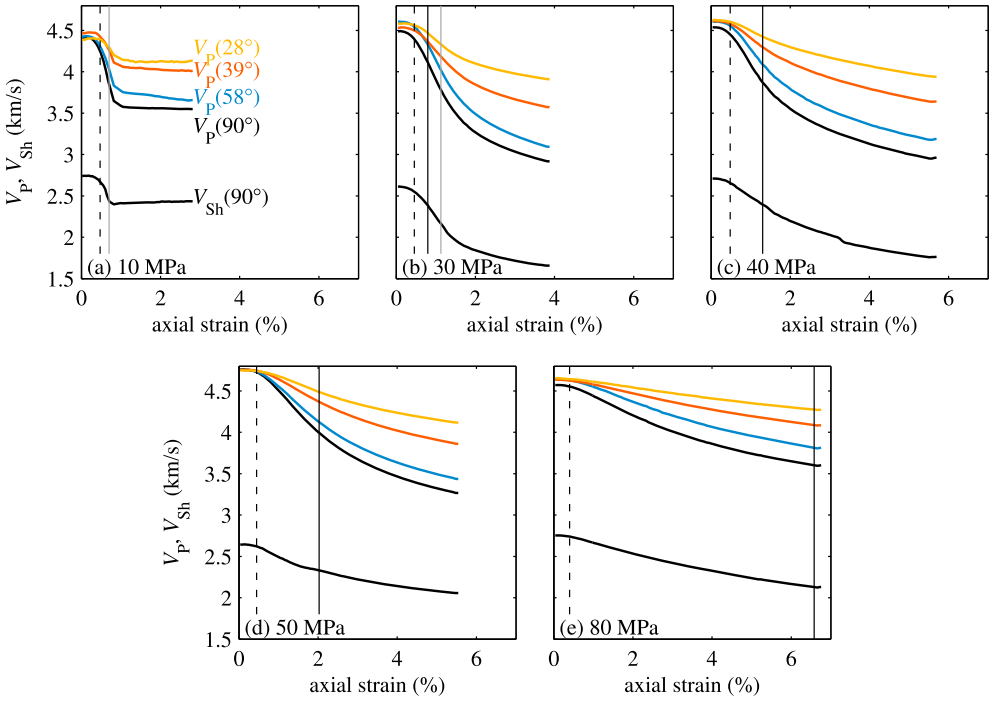


**Figure 4.** Evolution of *P* and *S* wave velocities as a function of axial strain during triaxial compression experiments performed at $P_{eff}$ = 10 (a), 30 (b), 40 (c), 50 (d), and 80 (e) MPa. Dashed lines mark the yield point (C′ in (a) and C* in (b–e)), black lines mark C*′, and grey lines mark the peak stress.

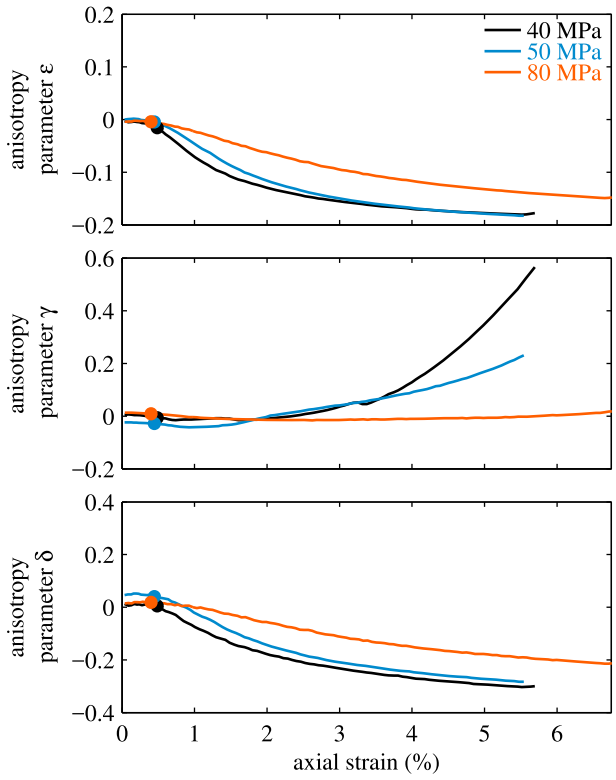


**Figure 5.** Thomsen's 1986 anisotropy parameters as a function of axial strain for the tests performed at 40-, 50-, and 80-MPa effective pressure. The filled circles mark the onset of inelastic compaction C*.

where $\rho$ is the density of the rock, $\theta$ is the propagation angle with respect to the symmetry axis (here assumed to be aligned with the compression axis), and

$$D^2(\theta) = \left[(C_{11} - C_{44})\sin^2(\theta) - (C_{33} - C_{44})\cos^2(\theta)\right]^2 + \left[(C_{13} + C_{44})\sin(2\theta)\right]^2. \quad (3)$$

Equation (2) is valid for horizontally polarized *S* waves, which is what is measured in our experiments. Using the *P* wave velocity measured at four independent angles with respect to the compression axis and the horizontal S wave velocity, we invert equations (1) and (2) for the elastic moduli $C_{11}$, $C_{33}$, $C_{44}$, $C_{66}$, and $C_{13}$ by a least squares method. This is done only for the experiments performed at $P_{eff}$ = 40, 50, and 80 MPa, where deformation remained homogeneous. Instead of presenting these results directly as a set of evolving elastic constants, it is more informative to compute anisotropy parameters and see how they evolve during deformation. Following Thomsen (1986), we compute the three independent parameters

$$\epsilon = (C_{11} - C_{33})/(2C_{33}), \quad (4)$$

$$\gamma = (C_{66} - C_{44})/(2C_{44}), \quad (5)$$

and

$$\delta = \frac{(C_{13} + C_{44})^2 - (C_{33} - C_{44})^2}{2C_{33}(C_{33} - C_{44})}. \quad (6)$$

The results are shown in Figure 5. The rock is initially essentially isotropic, and the onset of anisotropy coincides with the onset of inelastic compaction C*. The parameters $\epsilon$, which is the ratio of horizontal to vertical *P* wave velocities, and $\delta$, which characterizes the *P* wave anisotropy along the subvertical direction, decrease with increasing strain, down to values of the order of −0.2 to −0.3. The parameter $\gamma$, which quantifies the Sh wave anisotropy, remains small up to around 2 to 3% strain, beyond which it starts increasing with increasing strain (in the samples deformed at 40 and 50 MPa) or remains constant (at 80 MPa).

In order to test whether the wave velocities can be simply described in terms of an elliptical anisotropy, we plot the joined evolution of $\delta$ and $\epsilon$ in Figure 6. The ellipticity condition is $\delta = \epsilon$ (dashed line). We observe that all the data follow the same trend, which falls significantly below the ellipticity condition and can be approximated by a linear relationship between $\delta$ and $\epsilon$:

$$\delta \approx 1.8\epsilon. \quad (7)$$

The rock is therefore not well described by elliptical anisotropy, except maybe in the first 1% axial strain where the error made by assuming $\delta \approx \epsilon$ would be very small. The observation that $\delta < \epsilon < 0$ is entirely consistent with effective medium models for cracked materials containing fluid saturated vertical cracks (Guéguen & Sarout, 2009). Although the model used by Guéguen and Sarout (2009) is too simple to be used for our complex porous rock, the prediction of a decrease in $\delta$ and $\epsilon$ with increasing damage (with $\delta$ decreasing faster than $\epsilon$) is a consistent feature observed in our data. Thus, the increase in anellipticity of the wave velocities is unlikely to be specific to our particular rock type but rather a systematic feature found across most rocks undergoing cataclastic deformati on under triaxial conditions.

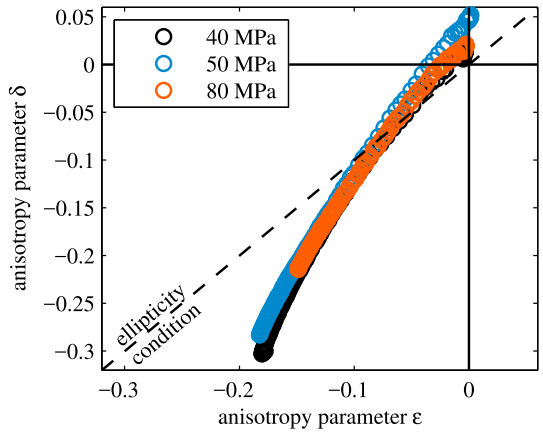


**Figure 6.** Anisotropy parameters $\delta$ and $\epsilon$ during deformation at $P_{eff}$ = 40, 50, and 80 MPa. The dashed line marks the condition $\delta = \epsilon$, for which the rock has a simple elliptical anisotropy.

The permeability change with increasing axial strain is displayed in Figure 7. In all experiments, the permeability initially decreases in the first 1% strain. In the brittle regime, the permeability increases after failure

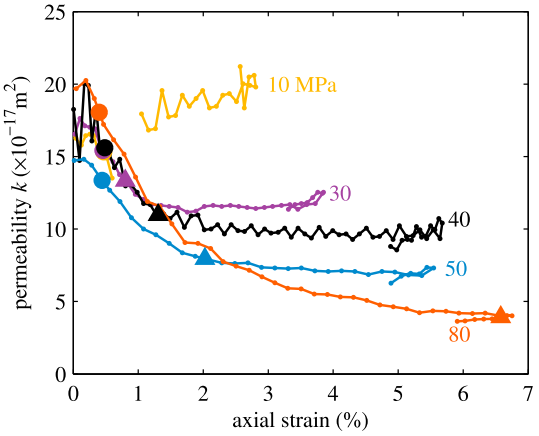


**Figure 7.** Evolution of permeability as a function of axial strain. The data gap in the test at $P_{eff}$ = 10 MPa corresponds to the time interval during which shear failure occurred and drainage conditions were uncertain. The filled circles correspond to the onset of inelastic compaction (C*), and the triangles to the onset of net dilation (C*′).

and returns to a value similar to that of the intact material. In the ductile regime ($P_{eff} \geq 30$ MPa), the permeability continues to decrease after the yield point and subsequently becomes stable beyond C*′. The overall changes in permeability are relatively modest, with the maximum decrease in $k$ from $2 \times 10^{-16}$ m$^2$ down to $4 \times 10^{-17}$ m$^2$ measured at $P_{eff}$ = 80 MPa after 6% strain.

The relative change in permeability $k/k_0$, where $k_0$ is the initial permeability of the sample prior to deformation, is shown as a function of porosity change in Figure 8. We observe a clear linear trend between permeability change and porosity change, common to all ductile experiments up to C*′. The trend is the same for the hydrostatic experiment. Beyond C*′, the permeability remains constant even though the overall porosity increases.

## 4. Microstructures

The microstructure of intact and deformed samples was investigated by scanning electron microscopy using backscattered electron mode. The intact rock (Figure 9) has macropores of around 50 μm in width located between large allochems (typically 100 to 200 μm in diameter). Allochems are made of microcrystalline calcite crystals, and porosity is distributed heterogeneously within them: both the center and the rims appear more porous (Figures 9a and 9b). The internal structure of the porous and compact parts of the allochems is shown in Figures 9c and 9d, respectively. The crystal size is typically below 1 μm, and locally much finer. In the compact areas, the grain boundaries appear very tight, and the rare micropores are located at triple junctions.

Representative microstructures of the sample deformed at $P_{eff}$ = 80 MPa, which underwent 6.7% axial strain and 2.1% compactant volumetric strain, are shown in Figures 10 and 11. An overall view of the microstructure at low magnification is given in Figure 10a. Macropores are clearly more scarce than in the intact sample, and microcracks are pervasively observed in both the cement crystals and in the low-porosity micrite. We find evidence for macropore collapse (Figure 10b), with tangential cracks surrounding the cavity that is partially filled with particles. The cement crystals tend to be cut through by thin straight cracks oriented parallel to the axis of compression, whereas the micrite appears to contain more diffuse, intergranular microcracks (Figure 10c). Most individual grains larger than around 5 to 10 μm in diameter are cracked and split (Figure 10d).

Close examination at high magnification confirms that large single crystals in the cement are heavily damaged by arrays of subvertical cracks (Figure 11a); but these intragranular cracks always arrest at the boundary between the cement and micrite (Figures 10c and 11b), where the rims of the allochem are more porous and fine grained. The low-porosity, compact areas of the micrite are systematically cracked (Figures 11b and 11c), forming tortuous paths across the areas where the low-porosity patches are large. At small scale, we find evidence of pervasive intergranular cracks (open grain boundaries) throughout the micrite (Figure 11d), mostly oriented parallel to the compression axis.

Overall, we observe three key microstructural features in the deformed samples: (1) macropore collapse, (2) thin, straight intragranular cracks in the cement, and (3) a diffuse network of intergranular cracks in the micrite, sometimes forming longer tortuous cracks where the micrite is less porous.

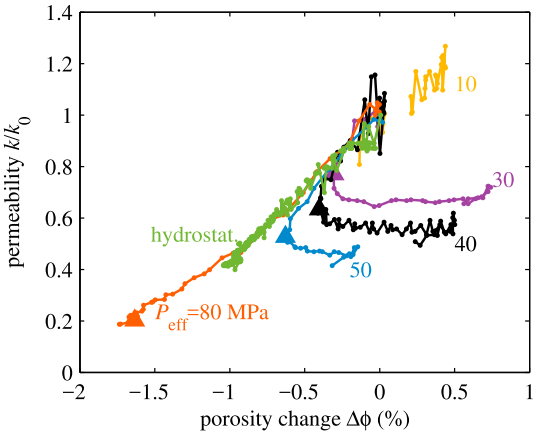


**Figure 8.** Relative change in permeability as a function of porosity change. Triangles mark the transition from net inelastic compaction to net dilation (C*′).

## 5. Discussion

### 5.1. Micromechanics of Inelastic Deformation

Our experiments show a decrease in elastic wave velocities during deformation in both the brittle and the ductile regime. This is in agreement with the existing data sets of Fortin et al. (2009) on a 17% porosity oolithic limestone and of Nicolas et al. (2016) on a 15% porosity micritic limestone.

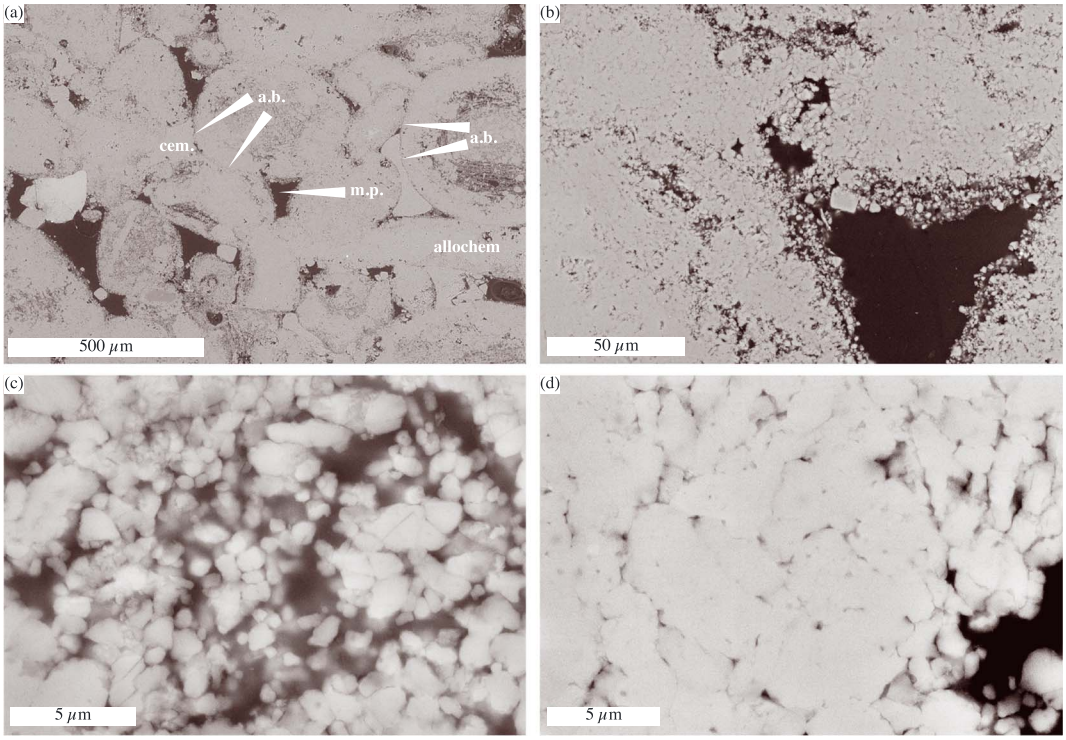


**Figure 9.** Scanning electron microscopy-backscattered electron images of intact Purbeck limestone. (a) Overview at low magnification showing macropores (m.p.), allochems (allochem boundary denoted a.b.) and calcite cement (cem.). (b) View of a macropore and of the microcrystalline calcite structure of the allochems. (c and d) Internal structure of the allochems, with submicron calcite crystals forming loose (c) or compact (d) aggregates.

The evolution of elastic wave velocities during hydrostatic compaction can be interpreted quantitatively in terms of crack density. Since the stress state is isotropic, we assume that the microcrack orientations remain isotropic. Here we use the differential effective medium approach with spheroidal saturated cracks (e.g., McLaughlin, 1977; Norris, 1985; Salganik, 1973; Zimmerman, 1991), which is based on the concept of sequentially introducing cracks in a homogeneous solid matrix and computing the effective properties of the matrix at each step. This approach allows us to account for interactions between cracks and other inhomogeneities in the rock. The bulk and shear moduli $(K, G)$ of the cracked material are computed as

$$\frac{1-\phi}{K}\frac{\mathrm{d}K}{\mathrm{d}\phi} = -(1-\zeta)P(\nu,\alpha,\zeta), \tag{8}$$

$$\frac{1-\phi}{G}\frac{\mathrm{d}G}{\mathrm{d}\phi} = -Q(\nu,\alpha,\zeta), \tag{9}$$

where $\phi$ is the porosity introduced in the material, $\nu$ is the Poisson's ratio, $\alpha$ is the aspect ratio of the spheroidal pores, and $\zeta = K_f/K$ is the ratio between the bulk modulus of the saturating fluid and that of the rock. The functions $P$ and $Q$ are the additional bulk and shear compliances of the spheroidal pores and are given in extenso by David and Zimmerman (2011). The pair of coupled differential equations (8) and (9) is solved numerically using the Runge-Kutta method. Here we take advantage of the differential approach and compute changes in crack density relative to a homogenized matrix having the average elastic properties measured on the rock at the highest pressure, that is, including all the remaining open porosity and other heterogeneities. Based on the measured velocities of $V_P = 4.73$ km/s and $V_S = 2.58$ km/s at $P_{eff} = 155$ MPa and using a density of $2.47 \times 10^3$ kg/m$^3$, we find initial bulk and shear moduli of $K_0 = 33.5$ GPa and $G_0 = 16.4$ GPa, respectively. For simplicity, we consider that all the cracks have the same "effective" aspect ratio and attempt to invert for both the crack density $\rho$, defined as $\rho = (3\phi)/(4\pi\alpha)$, and aspect ratio $(\alpha)$, using the measured $V_P$ and $V_S$ during hydrostatic compression. The inversion method is a full grid search where the most likely combination of $(\rho, \alpha)$ is found using the least absolute value criterion (Tarantola, 2005).

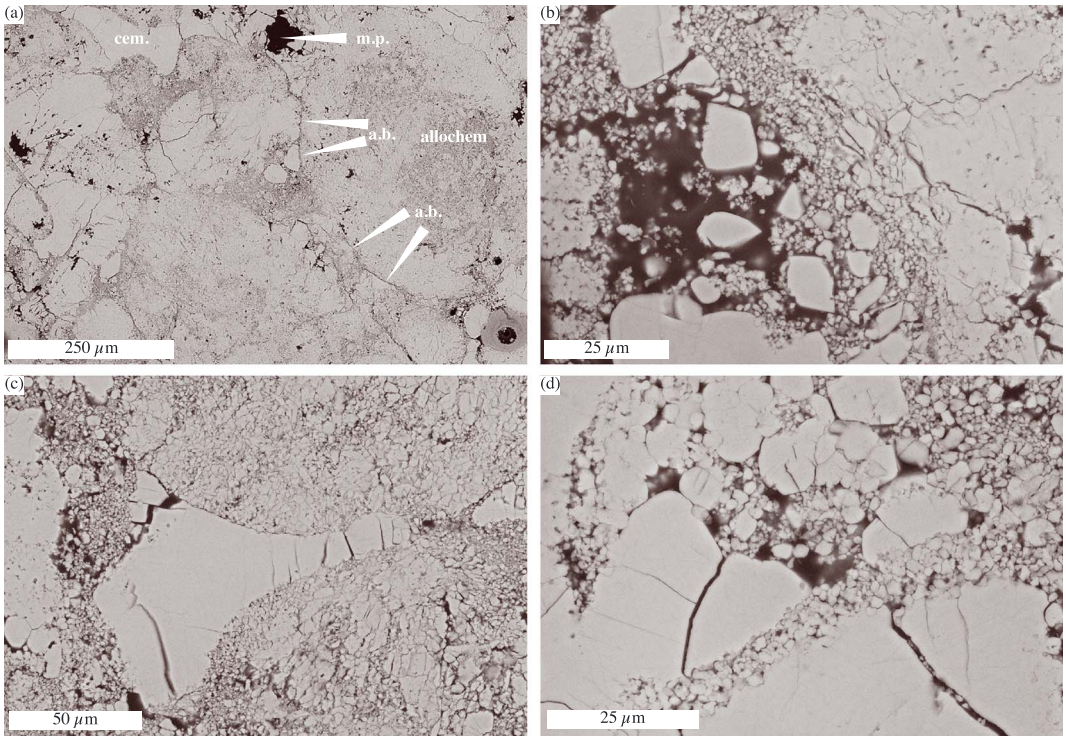


**Figure 10.** Scanning electron microscopy-backscattered electron images of Purbeck limestone deformed at $P_{eff} = 80$ MPa to 6.7% strain. The compression axis is vertical. (a) Overview at low magnification, showing cracked cement (cem.) and scarce remaining macropores (m.p.). Allochem boundaries (a.b.) are clearly visible. (b) Collapse of a macropore, surrounded by tangential microcracks and filled with particles. (c) Cracked calcite cement between allochems. (d) Cracked calcite crystals surrounded by microcrystalline allochem material.

The results for the change in crack density as a function of effective pressure and volumetric strain are presented in Figure 12. The inversion error in terms of aspect ratio is very large, and the inverted $\alpha$ are therefore not discussed here. By assumption, the crack density at the largest volumetric strain (achieved at the highest pressure $P_{eff} = 155$ MPa) is zero. The initial crack density relative to that state is around 0.08 and decreases rapidly to 0.03 at $P_{eff} = 55$ MPa. Above that pressure, the crack density decreases linearly with increasing pressure. Remarkably, P* (as inferred from the record of volumetric strain) is not marked by any specific variation in crack density. Along the unloading branch, the crack density gradually increases and deviates significantly from the loading branch at $P_{eff}$ around 90 MPa. The final crack density after unloading is 0.13. The difference between the loading and unloading path is best seen when the crack density is plotted as a function of the volumetric strain (Figure 12b), where we clearly observe that the crack density at a given strain is always higher during unloading than during loading.

It is clear from the velocity measurements and crack density inversion that a significant amount of microcrack damage appears in the rock under hydrostatic compression. However, this damage becomes visible only during unloading, which implies that either the cracks are formed during loading but remain closed above a threshold pressure or the cracks are created during unloading due to local strain incompatibilities accrued during plastic flow post-P*, which generate local stress concentration upon decompression. This behavior is in contrast with the typical drop in *P* and *S* wave velocities observed at P* in porous sandstones (Fortin et al., 2007), which correspond to grain crushing and pore collapse. In porous limestones, pore collapse is occurring primarily by so-called *cataclastic pore collapse* (e.g., Zhu et al., 2010), that is, microcracks initiating in the microporous surroundings of macropores. The lack of clear increase in crack density at P* indicates that only a minute amount of such microcracks is sufficient to trigger the collapse of macropores. Furthermore, the net irrecoverable strain after unloading was very small in our experiment (less than 0.2% volumetric strain), which indicates that only a modest amount of inelastic compaction and damaged occurred post-P*.

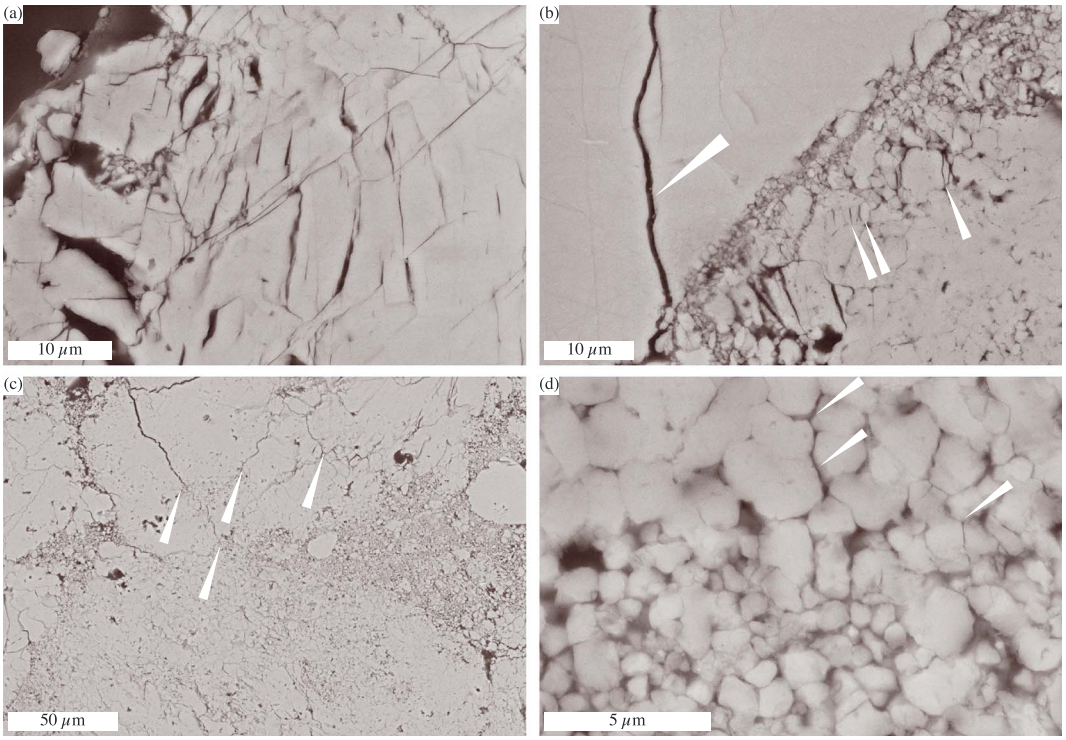


**Figure 11.** Scanning electron microscopy-backscattered electron images of Purbeck limestone deformed at $P_{eff}$ = 80 MPa to 6.7% strain. The compression axis is vertical. (a) Microcracks in the calcite cement. (b) Cracks (arrows) in the cement and in the allochems. (c) Structure of the allochem material, with tortuous cracks (arrows) in the compact aggregates. (d) Internal structure of the microcrystalline calcite aggregates, showing intergranular cracks (arrows).

In the dual porosity model of Zhu et al. (2010), the critical yield pressure P* is given as a function of porosity Φ as

$$P^* = \frac{0.883}{\Phi^{0.414}} S^*, \tag{10}$$

where $S*$ is a critical stress expressed as

$$S^* = \frac{K_{IC}}{(\Phi^*/\Phi)^{0.414}\sqrt{\pi a^*}}, \tag{11}$$

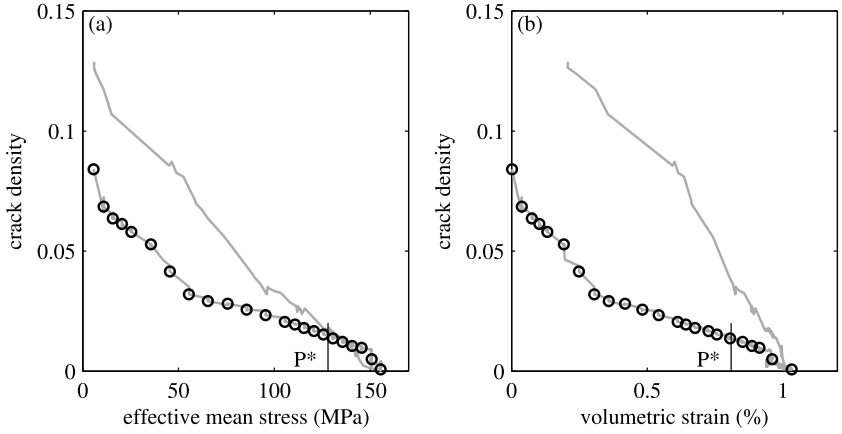


**Figure 12.** Crack density change as a function of volumetric strain during hydrostatic compression and decompression. The crack density is computed using the differential effective medium approach, using the elastic moduli measured at the highest pressure (i.e., largest volumetric strain) as the initial ones.

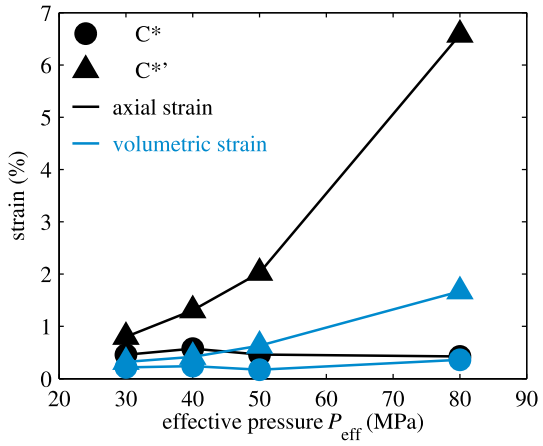


**Figure 13.** Axial and volumetric strain at the onset of inelastic compaction (C*) and net dilatancy (C*′), as a function of effective confining pressure.

where $\Phi^*$ is the porosity of the material surrounding macropores, $a^*$ is the size of the micropores, and $K_{IC}$ is the fracture toughness of the material. Using our picked value of $P^* = 128$ MPa and a porosity of 13.8%, we find that $S^* = 64$ MPa. The fracture toughness of calcite is around 0.2 MPa $m^{1/2}$ (Atkinson, 1984), and if we consider that the proportion of micropores $\Phi^*/\Phi \approx 0.95$ (see below), we find that the characteristic micropore size that explains the data is $a^* \approx 3$ μm. This size appears to be broadly consistent with the observed pore size in the micrite (Figures 9c and 9d).

The decrease in wave velocities during triaxial deformation experiments is clear evidence for microcrack growth during compaction. This is further confirmed by our microstructural investigations, showing microcracks in the cement and in the micrite. At the macroscopic scale, microcracking is also inferred from the observation of net dilatancy at strains beyond C*′. The amount of strain (both axial and volumetric) at C*′ is increasing with increasing confining pressure, as seen in Figure 13. This indicates an increasing amount of compaction with increasing confining pressure, while more shear strain is required for crack-induced dilatancy to overcome compaction.

One key question here is whether the amount of microcracks at the onset of net dilatancy (C*′) is similar between experiments performed under different pressure conditions. Due to the complex microstructure, large porosity, and anisotropy of the samples, it is difficult to perform any systematic inversion of the wave velocities into a quantitative crack density. To circumvent this issue, we use here the relative change in wave velocity as a proxy for microcrack damage. Figure 14 shows the relative change in the horizontal *P* and *Sh* wave velocities plotted as a function of the post-C* axial strain normalized by the strain at C*′. For all the tested confining pressures, we observe a clear collapse of the normalized curves onto a single downward trend. The relative decrease in both *P* and *S* wave velocities is of the order of 20% at C*′, regardless of the confining pressure. This indicates that the amount of microcracking at C*′ is similar for all our tests, hence showing that C*′ corresponds to a key microstructural state during cataclastic flow.

### 5.2. Permeability Evolution

The systematic decrease in permeability during inelastic compaction is proportional to the decrease in porosity (Figure 8) and is clearly at odds with the inferred increase in microcrack density. This implies that the microcracks produced during deformation are not significant pathways for the fluid.

Our microstructural observations indicate that the collapse of macropores is a significant contribution to the overall porosity reduction during ductile deformation. In order to assess the contribution of macropore collapse in the observed permeability reduction during deformation, we need to determine if macropores form a connected network for fluid flow in Purbeck limestone. Mercury injection porosimetry data (Wang et al., 2018) indicate that macropores only account for less than 5% of the total porosity. This is confirmed by 2-D macroporosity estimations performed by analyzing low magnification scanning electron microscopic images of intact Purbeck limestone, which indicate that pores of linear dimensions greater than 30 μm correspond only to a porosity of 5%. Purbeck limestone also shows many similarities to Indiana limestone in terms of microstructure, porosity and permeability, and X-ray computed microtomography studies. Ji et al. (2012) and Ji et al. (2015) showed that no connected backbone of macropores exists in Indiana limestone. Therefore, we conclude that the macroporosity is unlikely to form a connected network for permeability in our samples of Purbeck limestone.

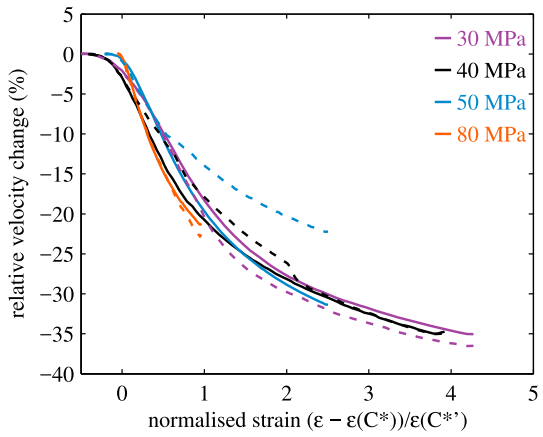


**Figure 14.** Relative change in horizontal *P* (solid lines) and *Sh* (dotted lines) wave velocities as a function of the postyield axial strain normalized by the strain at C*′.

The correlation between porosity and permeability reduction (Figure 8) cannot be simply interpreted as a causality, that is, the collapse of macropores within a connected backbone leading to a reduction in permeability. It is a different population of pores that play a role in the observed compaction and permeability reduction. According to mercury injection data

and our image analysis, Purbeck limestone has a microporosity of around 8 to 10%. One key outstanding goal is to determine whether all this microporosity contributes to a connected pore network for fluid flow, or if only a fraction of it does.

Modeling the microporous space as a connected network of pipes, the permeability can be expressed as (Guéguen & Dienes, 1989)

$$k = f\frac{r^2}{32}\Phi_p, \tag{12}$$

where $f$ is the percolation factor (equal to 1 in the fully connected regime), $r$ is the hydraulic aperture of the porosity, and $\Phi_p$ is the pipe porosity. For an average pipe length $\lambda$ and density $N$, the pipe porosity is given by

$$\Phi_p = N\pi r^2 \lambda, \tag{13}$$

so that permeability evolves as $k \propto r^4$. Our measurements (Figure 8) indicate a fivefold decrease in permeability during the test conducted at 80 MPa effective pressure, which is consistent with a decrease in $r$ by a factor 1.5. This implies that the pipe porosity has been reduced by a factor 2.2. The observed total change of porosity during compaction at 80 MPa effective pressure was 1.7%, but as explained above most of that compaction comes from the collapse of macropores, so that the collapse of micropores should amount to less than 1% porosity change. Therefore, the connected pipe porosity providing pathways for fluid flow is of the order of 2% at most. Since the permeability is of the order of $10^{-16}$ m$^2$, equation (12) implies that the hydraulic radius of the critical pipe porosity is at least of $r \gtrsim 0.5$ μm. This order of magnitude is consistent with the microstructural observations of intra-ooid porosity.

Overall, we conclude that only a small fraction of the microporosity contributes to the connected network that limits the permeability of Purbeck limestone. This conclusion is consistent with pore network models based on a critical path analysis (e.g., Katz & Thompson, 1986), where permeability is controlled by the fraction of the porosity having hydraulic radius above a critical threshold.

The proportionality between permeability and porosity reduction therefore reflects that macropores and micropores are collapsing in similar proportions during deformation, but that only macropores contribute significantly to the total porosity change, while only a fraction of the largest micropores contribute to the total permeability change.

One key additional observation is the stabilization of permeability beyond C*′, even during unloading. From a phenomenological point of view, the residual permeability value scales with the maximum compaction achieved during the tests and is therefore a decreasing function of the applied confining pressure. At the microscale level, it implies that the dilatant microcracks do not modify the main backbone of micropores that provides pathways for the fluid, even though this backbone has undergone significant compaction. Therefore, we conclude that the micropore network controlling the permeability of the rock is at an intermediate scale between the macropores (>30 μm) and the main network of micropores and microcracks (<0.5 μm).

## 6. Conclusion

Overall, our experimental data show that deformation in the ductile regime induces (1) the compaction of the macroporosity, followed by net dilation due to crack growth in the cement and microporous micrite, (2) an irreversible permeability reduction proportional to the amount of compaction, and (3) a decrease in wave velocity and the generation of a strong anelliptic elastic anisotropy.

Similar to the case of porous sandstones, the collapse of macroporosity itself is not expected to produce any increase in wave velocities, since pores of equant shapes have only a minor effect on elastic properties compared to thin cracks (e.g., Shafiro & Kachanov, 1997). By contrast, the generation of microcracks during inelastic compaction, while having a negligible impact on permeability, has a first-order impact on the elastic properties and produces a strong decrease in moduli together with an anisotropy with a symmetry given by the axis of compression (here, mostly subvertical cracks). The growth of microcracks is promoted by the easy cleavage of calcite single crystals in the cement and by the micropores in the micrite that concentrate stresses around them.

During hydrostatic compaction, our experiments show that microcracks are likely not formed during loading. The modest inelastic compaction appears to arise from the collapse of macroporosity but the continuous

decrease in crack density indicates that little to no new cracks are formed there. The strong increase in crack density inferred upon unloading is possibly due to the generation of stress concentrations from twins and dislocation pileups accumulated in the loading stage, which is consistent with previous observations and models (Baud et al., 2000; Vajdova et al., 2012).

The complex behavior of porous limestones during compaction arises from both their complex microstructure (with a dual porosity) and the semibrittle behavior of calcite itself, which has active twinning and slip systems at room temperature. This complexity is in contrast with porous sandstones, which are typically well described by granular mechanics (e.g., Fortin et al., 2007; Guéguen & Fortin, 2013; Zhang et al., 1990).

The decrease in permeability due to compaction and the decrease in wave velocities due to crack growth highlights the key role of the multiscale aspect of porosity in the physical properties of limestones. The macroporosity formed by the space between the allochems and cement essentially controls the potential of bulk compaction because it can be easily compacted at relatively low stresses, but it is not interconnected and thus does not provide pathways for fluids. The permeability is controlled by a small fraction of the microporosity within the allochems, and we infer that this fraction consists in pores having a critical hydraulic radius of at least 0.5 μm. The remaining microporosity, which dominates the total porosity of the rock, does not seem to play any role in the transport properties or bulk compaction. However, this pervasive microporosity acts as a network of defects from which microcracks, dislocations, and twins can nucleate and therefore controls the deformation mechanisms. In conclusion, we have shown here that the complex microstructure, the wide size distribution of porosity, and the semiplastic behavior of calcite creates a disconnection between the evolution of porosity, permeability, and elastic properties during compaction deformation of porous limestone.

Here we only investigated one rock, Purbeck limestone, which was taken as a representative for porous allochemical limestones. However, systematic observations on a wider range of limestones with different microstructures are required to draw further quantitative conclusions on the respective role of crystal plasticity, dual porosity, and other microstructural features. As recently evidenced by Regnet et al. (2015), what may appear as details in the microstructures, such as the spatial distribution of the microporosity in the micrite, can potentially have a significant impact on the mechanical and transport properties of the rock.

The deformation mechanisms investigated here are all related to crack growth, pore collapse, and/or crystal plasticity. In the presence of water, porous limestones are also expected to deform by stress-activated dissolution-precipitation processes, especially at low strain rates (e.g., Brantut et al., 2014b; Zhang & Spiers, 2005). Dissolution-precipitation phenomena have the potential to reduce porosity and seal microcracks (e.g., Richard et al., 2015) and therefore are coupled to the deformation-induced crack growth and pore collapse processes described in our samples. Because of potentially complex feedbacks between dissolution-precipitation and microcracking processes, it is difficult to assess a priori how the presence of aqueous pore fluids would affect the long-term behavior of porous limestones. Clearly, further work in needed in this direction.

**Acknowledgments**
This work was supported by the UK Natural Environment Research Council through grant NE/K009656/1 to N. B. Emmanuel C. David is gratefully acknowledged for his help in using the differential effective medium scheme. We thank Harry Lisabeth and Marco Scuderi for their review comments that helped clarify the paper. The data used in this paper are freely available from the UK National Geoscience Data Centre (http://www.bgs.ac.uk/services/ngdc/accessions/index.html#item110229) or upon request to the corresponding author.

## References

Angerer, E., Crampin, S., Li, X.-Y., & Davis, T. L. (2002). Processing, modelling and prediction time-lapse effects of overpressured fluid-injection in a fractured reservoir. *Geophysics*, *149*(2), 267–280.

Anselmetti, F. S., Luthi, S., & Eberli, G. P. (1998). Quantitative characterization of carbonate pore systems by digital image analysis. *AAPG Bulletin*, *82*(10), 1815–1836.

Atkinson, B. K. (1984). Subcritical crack growth in geological materials. *Journal of Geophysical Research*, *89*(B6), 4077–4114.

Baechle, G. T., Colpaert, A., Eberli, G. P., & Weger, R. J. (2008). Effects of microporosity on sonic velocity in carbonate rocks. *Leading Edge*, *27*, 1012–1018. https://doi.org/10.1190/1.2967554

Baud, P., Exner, U., Lommatzsch, M., Reuschlé, T., & Wong, T.-F. (2017). Mechanical behavior, failure mode, and transport properties in a porous carbonate. *Journal of Geophysical Research: Solid Earth*, *122*, 7363–7387. https://doi.org/10.1002/2017JB014060

Baud, P., Meredith, P. G., & Townend, E. (2012). Permeability evolution during triaxial compaction of an anisotropic porous sandstone. *Journal of Geophysical Research*, *117*, B05203. https://doi.org/10.1029/2012JB009176

Baud, P., Schubnel, A., Heap, M. J., & Rolland, A. (2017). Inelastic compaction in high porosity limestone monitored using acoustic emissions. *Journal of Geophysical Research: Solid Earth*, *122*, 9989–10,009. https://doi.org/10.1002/2017JB014627

Baud, P., Schubnel, A., & Wong, T.-F. (2000). Dilatancy, compaction, and failure mode in Solnhofen limestone. *Journal of Geophysical Research*, *105*(B8), 19,289–19,303.

Bernabé, Y., Mok, U., & Evans, B. (2006). A note on the oscillating flow method for measuring rock permeability. *International Journal of Rock Mechanics and Mining*, *43*(2), 311–316.

Brantut, N., Heap, M. J., Baud, P., & Meredith, P. G. (2014a). Rate- and strain-dependent brittle deformation of rocks. *Journal of Geophysical Research: Solid Earth*, *119*, 1818–1836. https://doi.org/10.1002/2013JB010448

Brantut, N., Heap, M. J., Baud, P., & Meredith, P. G. (2014b). Mechanisms of time-dependent deformation in porous limestone. *Journal of Geophysical Research: Solid Earth*, *119*, 5444–5463. https://doi.org/10.1002/2014JB011186

Choquette, P. W., & Pray, L. C. (1970). Geologic nomenclature and classification of porosity in sedimentary carbonates. *AAPG Bulletin*, *54*(2), 207–250.

Dautriat, J., Gland, N., Dimanov, A., & Raphanel, J. (2011). Hydromechanical behavior of heterogeneous carbonate rock under proportional triaxial loadings. *Journal of Geophysical Research*, *116*, B01205. https://doi.org/10.1029/2009JB000830

David, E. C., & Zimmerman, R. W. (2011). Compressibility and shear compliance of spheroidal pores: Exact derivation via the Eshelby tensor, and asymptotic expressions in limiting cases. *International Journal of Solids and Structures*, *48*, 680–686.

Eccles, D., Sammonds, P. R., & Clint, O. C. (2005). Laboratory studies of electrical potential during rock fracture. *International Journal of Rock Mechanics and Mining Sciences*, *42*(7-8), 933–949.

Fischer, G. J., & Paterson, M. S. (1992). Measurement of permeability and storage capacity in rocks during deformation at high temperature and pressure. In B. Evans & T. F. Wong (Eds.), *Fault mechanics and transport properties of rocks, International geophysics series* (pp. 187–211). London: Academic Press.

Fortin, J., Guéguen, Y., & Schubnel, A. (2007). Effects of pore collapse and grain crushing on ultrasonic velocities and $v_p/v_s$. *Journal of Geophysical Research*, *112*, B08207. https://doi.org/10.1029/2005JB004005

Fortin, J., Stanchits, S., Dresen, G., & Guéguen, Y. (2009). Micro-mechanisms involved during inelastic deformation of porous carbonate rocks. In *Proceedings of the Fourth Biot Conference on Poromechanics* (pp. 378–383). New York: Columbia University.

Grochau, M. H., Monteiro Benac, P., de Magalhães Alvim, L., Sansonowski, R. C., da Motta Pires, P. R., & Villaudy, F. (2014). Brazilian carbonate reservoir: A successful seismic time-lapse monitoring study. *Leading Edge*, *33*(2), 164–166.

Guéguen, Y., & Dienes, J. (1989). Transport properties of rocks from statistics and percolation. *Mathematical Geology*, *21*(1), 1–13.

Guéguen, Y., & Fortin, J. (2013). Elastic envelopes of porous sandstones. *Geophysical Research Letters*, *40*, 3550–3555. https://doi.org/10.1002/grl.50676

Guéguen, Y., & Sarout, J. (2009). Crack-induced anisotropy in crustal rocks: Predicted dry and fluid-saturated Thomsen's parameters. *Physics of the Earth and Planetary Interiors*, *172*, 116–124.

Ji, Y., Baud, P., Vajdova, V., & Wong, T.-F. (2012). Characterization of pore geometry of indiana limestone in relation to mechanical compaction. *Oil & Gas Science and Technology–Revue d'IFP Energies nouvelles, Institut Français du Pétrole*, *67*(5), 753–775.

Ji, Y., Hall, S. A., Baud, P., & Wong, T.-F. (2015). Characterization of pore structure and strain localization in Majella limestone by X-ray computed tomography and digital image correlation. *Geophysical Journal International*, *200*, 699–717.

Katz, A. J., & Thompson, A. H. (1986). Quantitative prediction of permeability in porous rock. *Physical Review B*, *34*(11), 8179–8181.

Lisabeth, H. P., & Zhu, W. (2015). Effect of temperature and pore fluid on the strength of porous limestone. *Journal of Geophysical Research: Solid Earth*, *120*, 6191–6208. https://doi.org/10.1002/2015JB012152

McLaughlin, R. (1977). A study of the differential scheme for composite materials. *International Journal of Engineering Science*, *15*, 237–244.

Nicolas, A., Fortin, J., Regnet, J. B., Dimanov, A., & Guéguen, Y. (2016). Brittle and semi-brittle behaviours of a carbonate rock: Influence of water and temperature. *Geophysical Journal International*, *206*, 438–456. https://doi.org/10.1093/gji/ggw154

Nicolas, A., Fortin, J., Regnet, J. B., Verberne, B. A., Plümper, O., Dimanov, A., et al. (2017). Brittle and semibrittle creep of Tavel limestone deformed at room temperature. *Journal of Geophysical Research: Solid Earth*, *122*, 4436–4459. https://doi.org/10.1002/2016JB013557

Norris, A. N. (1985). A differential scheme for the effective moduli of composites. *Mechanics of Materials*, *4*, 1–16.

Pittman, E. D. (1971). Microporosity in carbonate rocks. *AAPG Bulletin*, *55*(10), 1873–1878.

Regnet, J. B., David, C., Fortin, J., Robion, P., Makhloufi, P., & Collin, P.-Y. (2015). Influence of microporosity distribution on the mechanical behavior of oolithic carbonate rocks. *Geomechanics for Energy and the Environment*, *3*, 11–23.

Richard, J., Doan, M.-L., Gratier, J.-P., & Renard, F. (2015). Microstructures induced in porous limestone by dynamic loading, and fracture healing: An experimental approach. *Pure and Applied Geophysics*, *172*, 1269–1290.

Salganik, R. L. (1973). Mechanics of bodies with many cracks. *Mechanics of Solids*, *8*(4), 135–143.

Shafiro, B., & Kachanov, M. (1997). Materials with fluid-filled pores of various shapes: Effective elastic properties and fluid pressure polarization. *International Journal of Solids and Structures*, *34*(27), 3517–3540.

Tarantola, A. (2005). *Inverse problem theory* (2nd ed.). Philadelphia: Society for Industrial Mathematics.

Thomsen, L. (1986). Weak elastic anisotropy. *Geophysics*, *51*(10), 1954–1966.

Vajdova, V., Baud, P., & Wong, T.-F. (2004). Compaction, dilatancy, and failure in porous carbonate rocks. *Journal of Geophysical Research*, *109*, B05204. https://doi.org/10.1029/2003JB002508

Vajdova, V., Baud, P., Wu, L., & Wong, T.-F. (2012). Micromechanics of inelastic compaction in two allochemical limestones. *Journal of Structural Geology*, *43*, 100–117.

Wang, Y., Meng, F., Wang, X., Baud, P., & Wong, T.-F. (2018). Effective stress law for the permeability and deformation of four porous limestones. *Journal of Geophysical Research: Solid Earth*, *123*. https://doi.org/10.1029/2018JB015539

Wong, T.-F., & Baud, P. (2012). The brittle-ductile transition in porous rock: A review. *Journal of Structural Geology*, *44*, 25–53.

Zhang, X., & Spiers, C. J. (2005). Compaction of granular calcite by pressure solution at room temperature and effects of pore fluid chemistry. *International Journal of Rock Mechanics and Mining Sciences*, *42*, 950–960.

Zhang, J., Wong, T.-F., & Davis, D. M. (1990). Micromechanics of pressure-induced grain crushing in porous rocks. *Journal of Geophysical Research*, *95*(B1), 341–351.

Zhu, W., Baud, P., & Wong, T.-F. (2010). Micromechanics of cataclastic pore collapse in limestone. *Journal of Geophysical Research*, *115*, B04405. https://doi.org/10.1029/2009JB006610

Zhu, W., & Wong, T.-F. (1997). The transition from brittle faulting to cataclastic flow: Permeability evolution. *Journal of Geophysical Research*, *102*(B2), 3027–3041.

Zimmerman, R. W. (1991). Elastic moduli of a solid containing spherical inclusions. *Mechanics of Materials*, *12*, 17–24.